



A novel framework for seamless mosaic of Cartosat-1 DEM scenes[☆]

Rajeshreddy Datla^{a,b,*}, C. Krishna Mohan^b

^a Signal processing division, Advanced Data Processing Research Institute (ADRIN), Department of Space, Akbar Road, Tarbunde, Manovikas Nagar, Secunderabad 500009, India

^b Visual Learning and Intelligence Group (VIGIL), Department of Computer Science and Engineering, Indian Institute of Technology Hyderabad (IITH), Kandi, Sangareddy, Hyderabad 502285, India

ARTICLE INFO

Keywords:

Cartosat-1
Digital elevation model
Mosaic
Feathering-based blending
Order of precedence
Traversal algorithm
Photogrammetry

ABSTRACT

Digital elevation model (DEM) is used as a source of elevation data in wide range of applications. The applications involving larger area than an individual DEM scene often need a mosaic of DEM scenes. A simple stitching exhibits seams along the borders of DEM scenes in the mosaic output. The presence of seam lines varies with the number of scenes in an overlapping region and their overlap extents. The conventional feathering-based blend method, by virtue of the method itself, considers only two input scenes in an instance of the mosaic process. This method requires a suitable ordering of the input DEM scenes, especially in the overlapping regions containing more than two scenes. In this paper, we propose a framework that automatically handles the multiple overlapping regions and creates a seamless mosaic of Cartosat-1 DEM scenes for a given region of interest. We use a tree data structure to arrange input DEM scenes hierarchically based on their metadata. A traversal algorithm is devised to establish an order of precedence among the DEM scenes. This determines a unique input sequence of DEM scenes during mosaic process. In addition, two variants of feathering-based blend method are formulated to handle all possible cases of the overlapping regions. The experiments have been conducted on Cartosat-1 DEM scenes over $1^\circ \times 1^\circ$ region of interest. We analyze and compare our proposed methodology with average method and feathering-based blend method. We demonstrate that our framework exhibits a smooth transition of elevation values in the overlapping regions of the DEM mosaic output.

1. Introduction

The digital elevation model (DEM) is the digital representation of the surface of the earth. It is a crucial input for tasks such as ortho-image generation, topographic mapping (Amitabh et al., 2008; Radhadevi et al., 2009; Binoy et al., 2014), watershed extraction (Simhadri et al., 2013; Prashantha, 2017; Ramesh et al., 2017; Aher et al., 2017), spatial decision support system (Pal and Saha, 2017), and better image interpretation (Dahatonde et al., 2016). The DEM is also widely considered for source of elevation data in various applications such as disaster management (Martha et al., 2010; Buhler et al., 2013; Dong and Shan, 2013; Bhardwaj et al., 2014; Sharma and Kartikeyan, 2014; Bhatt and Rao, 2016), urban planning (Bhandari et al., 2006; Rao et al., 2007), infrastructural studies (Geiss et al., 2015), change detection (Tian et al., 2013), surface reconstruction (Tack et al., 2012), virtual 3D display (Amitabh et al., 2009; Rajpriya et al., 2014; Steve

and Heidrun, 2017), fly through, visibility analysis, etc. Applications involving large study area, often needs seamless mosaic of DEM scenes preferably with better vertical accuracy. High resolution DEMs are also helpful in separating foreground objects from background.

Cartosat-1 is a unique Indian remote sensing (IRS) satellite that has along track optical stereo imaging capability with 2.5 m resolution (NRSC, 2015). The Cartosat-1 mission has a systematic coverage with its own referencing scheme, named path-row, described in NRSA (2006). The acquisition of consecutive paths has a separation of eleven days with an overlap of approximately 10%. The stereo pairs acquired by this mission are considered to generate DEM scenes of size 27.5 km \times 27.5 km (Jacobsen et al., 2008; Jain et al., 2008). The systematic coverage of the Cartosat-1, described in NRSA (2006) is favorable to create a global DEM, which is the primary goal of the mission. Nevertheless, mosaic is required if the region of interest exceeds an

[☆] Code is available at <https://www.github.com/RAJESH/DAT/ Cartosat-1-DEM-Mosaic>.

* Corresponding author at: Signal processing division, Advanced Data Processing Research Institute (ADRIN), Department of Space, Akbar Road, Tarbunde, Manovikas Nagar, Secunderabad 500009, India.

E-mail addresses: rajesh@adrin.res.in (R. Datla), ckm@iith.ac.in (C.K. Mohan).

URL: <http://www.iith.ac.in/~ckm> (C.K. Mohan).

individual DEM scene. DEM mosaic is the alignment of multiple overlapping DEM scenes into a large composition. The process of DEM mosaic considers systematic correction of the individual DEM scenes as the preliminary task. These systematic errors inherently present due to the acquisition of stereo pairs from different orbits, different seasons, and different viewing geometries (NRSC, 2013; Amitabh et al., 2011; Giribabu, 2014) of Cartosat-1 mission. The correction mechanisms are helpful merely to minimize the systematic errors, if any, in individual DEM scenes. A simple stitching would apparently introduce seams in the borderline of the overlapping regions (Jain et al., 2008), though their elevation values are within the threshold of vertical accuracy. Hence, a methodology is required to create a seamless DEM mosaic for better interpretation of the terrain.

The *feathering-based blend* and *average* methods are the available blending methods suited for raster data sets such as DEM scenes (ESRI, 2011). However, these methods are different in the way they assign weights to the cells of DEM scenes in the overlapping region. The *average* method is convenient, but it typically introduces discontinuities (Reuter et al., 2009; Robinson et al., 2014) in the borders of the overlapping regions. The *feathering-based blend method* is considered superior (Ghosh and Kaabouch, 2016) among the mosaic methods in the image processing domain. This method has a limitation on scalability, though it performs reasonably well for two inputs. Here, scalability is the ability to handle more than two inputs available in an overlapping region simultaneously. This property is constrained by nature of the method itself, as described in Milgram (1975, 1977) and Hsu and Wu (1996), which considers only two inputs in an instance of mosaic process. In DEM mosaic process, the number of input DEM scenes in an overlapping region typically varies from two to four and they may belong to same path or two consecutive paths. The DEM scenes of same path with an overlap are termed *end-lap* and scenes with an overlap in consecutive paths are termed *side-lap* (Wilkinson et al., 2014). In either case of end-lap or side-lap, the feathering-based blend method produces seamless mosaic outputs, irrespective of the ordering of DEM scenes during mosaic process. However, in case of overlapping region with more than two DEM scenes, the mosaic output vary with the ordering of DEM scenes. This necessitates explicit ordering of DEM scenes during mosaic process using feathering-based blend method, especially in the overlapping regions with more than two DEM scenes. On the contrary, average method does not require an ordering, as it simply averages the elevation values by considering all the DEM scenes of the overlapping region at a time.

In this work, we use feathering-based blend method for mosaic of Cartosat-1 DEM scenes. This method performs the mosaic process by considering two DEM scenes iteratively from the input list in an instance. The ordering of scenes in this list is based on date and time of their stereo-pairs acquisition. The mosaic output obtained from this conventional feathering-based blend method exhibits seam lines in the overlapping regions. This may have influenced by an inappropriate ordering of input scenes during mosaic process. We use a traversal algorithm to determine a unique hierarchical input sequence among the input DEM scenes based on their metadata. The ordering of scenes from this input sequence is considered iteratively by feathering-based blend method. This eliminates the presence of seam lines in the overlapping regions. The novel contribution of this work is to provide a unique input sequence to the feathering-based blend method in manifesting seamless DEM mosaic output.

The rest of this paper is organized as follows. Section 2 provides a brief review of existing methods for DEM mosaic creation. In Section 3, we present the proposed framework in detail. The experimental results and their analysis are discussed in Section 4. Finally, we conclude this paper in Section 5.

2. Related work

A simple stitching of the DEM scenes, even after registration, exhibits visible differences in the mosaic output. These differences vary

with the number of DEM scenes and their elevation inconsistencies, particularly in the overlapping regions. Nevertheless, registration and blending are the two significant steps that mainly influence the quality of DEM mosaic output, as stated in Ghosh and Kaabouch (2016). Blending computes a new elevation value for each cell in the overlapping region from multiple elevation values. The smoothness depends largely on the weights assigned to each cell in the overlapping region during computation of new elevation values. A suitable weight derivation mechanism in the blending is required to minimize the visible differences in the overlapping regions. In this section, we briefly review the existing blending methods based on weight derivation mechanisms used in creating a seamless DEM mosaic.

2.1. Average method

This method simply averages multiple elevation values of each cell in the overlapping regions. The shuttle radar topography mapper (SRTM) mission, in late 1999, aimed to create DEMs with global coverage. It considered multi-source DEM scenes, such as interferometric synthetic aperture radar (InSAR) from SRTM, and TanDEM data from European remote sensing (ERS) for mosaic. Systematic errors are corrected (Käöpfler et al., 1998) based on height error maps estimated from the accuracies of the input DEMs. Statistical tests on outliers are also performed additionally, to remove gross errors in the individual DEMs. Finally, the conventional average method is used to create the DEM with global coverage. The Geocoding and Mosaicking System (GeMoS) (Roth et al., 1999) is an advanced system to Käöpfler et al. (1998), which has an additional geocoding process. However, this system specifically considers the DEMs from an advanced synthetic aperture radar (ASAR) along with SRTM and uses average method in the mosaic process.

TerraSAR-X add-on for digital elevation measurement (TanDEM-X) is another mission for the derivation of DEM with global coverage described (Astrid et al., 2016). A single-pass SAR interferometry (Krieger et al., 2007; Zink et al., June 2014) obtained from TanDEM-X and TerraSAR-X are used for the generation of DEMs. The discrepancies in their elevation values are mainly due to the errors from phase unwrapping or different temporal acquisitions. The block adjustment is performed to correct the inconsistencies in the individual DEMs. Finally, average method is able to further minimize the remained systematic errors.

2.2. Distance-weighted method

This method derives weights based on the distance from the cells to the borderline in the overlapping region. These weights are used to adjust the elevation values of the cells in the overlapping regions. The DEM mosaic method described in Warriner and Mandlbürger (2005) is based on a tolerance band. This band is determined by marking the boundaries manually over the two DEM scenes. The weights are derived based on the distance of a cell from either side of the center line of the tolerance band. The suitable weights can be derived to obtain a seamless DEM mosaic by changing its tolerance band accordingly. The drawback of this method is due to the manual marking of its tolerance band.

2.3. First and last methods

These methods do not process the cell values except copying elevation values. In the first method, the mosaic output has elevation values from the first DEM in the input list. Similarly in the last method, elevation values are copied from the last DEM. A modified blend method (MBlend) is described in Leitão et al. (2016) to merge two DEMs with different resolutions. MBlend generates a raster surface that represents the elevation differences between these two DEMs. This

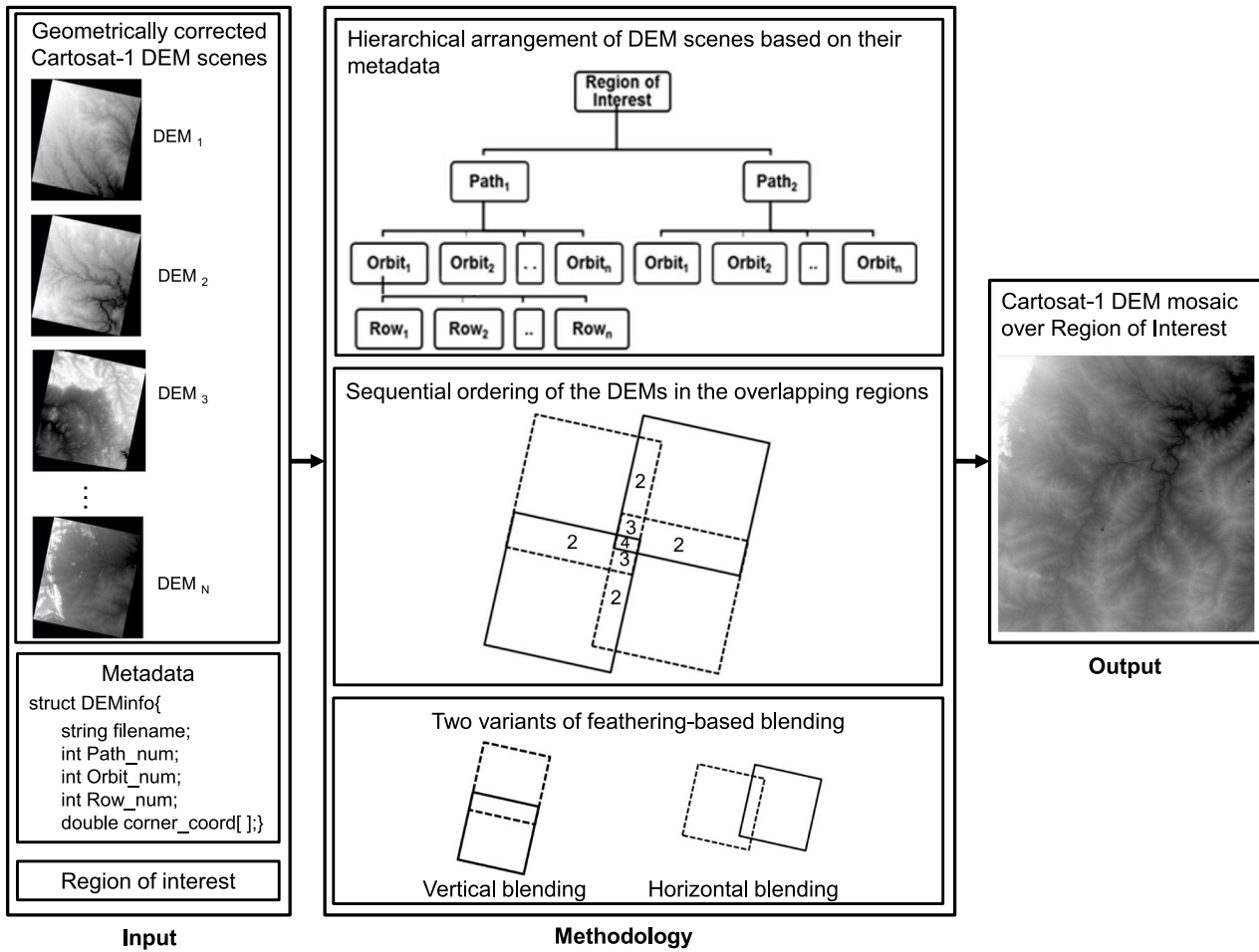


Fig. 1. Block diagram of the proposed framework for a seamless mosaic of Cartosat-1 DEM scenes.

surface is considered as a weight map which is added to the low-resolution DEM such as cartographic DEM by retaining high resolution DEM from airborne LiDAR. Mblend uses a cover method by considering the high-resolution DEM as first DEM (top DEM) followed by the modified low-resolution DEM as last DEM (bottom DEM) in the mosaic process. These methods are useful to select the elevation values from the DEMs of better quality in a given input list.

Most of the existing mosaic methods used average and distance based algorithms in the weight derivation mechanisms. We compare these two methods with the proposed method with a specific ordering of input scenes during the mosaic. In general, mosaic process involves input DEM scenes from different orbits, seasons, and viewing geometry. An overlapping region contains more than two DEMs that requires a mechanism to order them for the subsequent mosaic process. The methods in the literature do not consider an order of precedence among the DEMs in the overlapping regions during the mosaic process. In this paper, we formulate the sequential ordering mechanism using their metadata during the mosaic process. We also introduce two variants of feathering-based blend method to address various cases of overlapping regions of the DEMs.

3. Proposed framework

The block diagram of the proposed framework for seamless mosaic of Cartosat-1 DEM scenes is shown in Fig. 1. The proposed framework considers Cartosat-1 DEM scenes, their metadata, and extents to define a region of interest as input. These DEM scenes considered, in this work, are systematically corrected using bundle block adjustment (BBA) software (Akilan et al., 2014). This ensures continuity in the

geometry of the DEM scenes and allows us to skip the DEM registration and the re-projection steps in this work. The methodology consists of three components, namely, metadata based schematic arrangement of the input DEM scenes, sequential ordering of the DEM scenes during the mosaic process, and two variants of feathering-based blend method. These three components are explained in the subsequent subsections in detail.

3.1. Metadata based schematic representation

The referencing scheme of Cartosat-1, which is described in NRSA (2006), provides a convenient way to identify a geographic location on the earth. This scheme designates path and row numbers for image referencing corresponding to a ground location. A path refers to a descending ground trace of an orbit. A row refers to a scene, which is segmented from the continuous stream of a path. The path number followed by row number merely locates an input scene center. This referencing scheme determines 1867 total paths numbered from west to east and 785 rows for each path to have complete index of the earth. The orbit number, path number, row number, and time of acquisition are included as metadata to uniquely identify an input DEM scene.

We consider the metadata of input DEM scenes to arrange them hierarchically as shown in Fig. 2. A four-level tree represents the input DEM scenes based on their metadata. The region of interest (ROI) is considered as the root (Level 0) of the tree. Level 1, Level 2, and Level 3 represent path numbers, orbit numbers, and row numbers (leaf nodes) denoted by $\{Path_k\}_{k=1}^p$, $\{Orbit_j\}_{j=1}^m$, and $\{R_i\}_{i=1}^n$, respectively. A row R_i of $\{R_i\}_{i=1}^n$ indicates an input DEM scene. The total number of

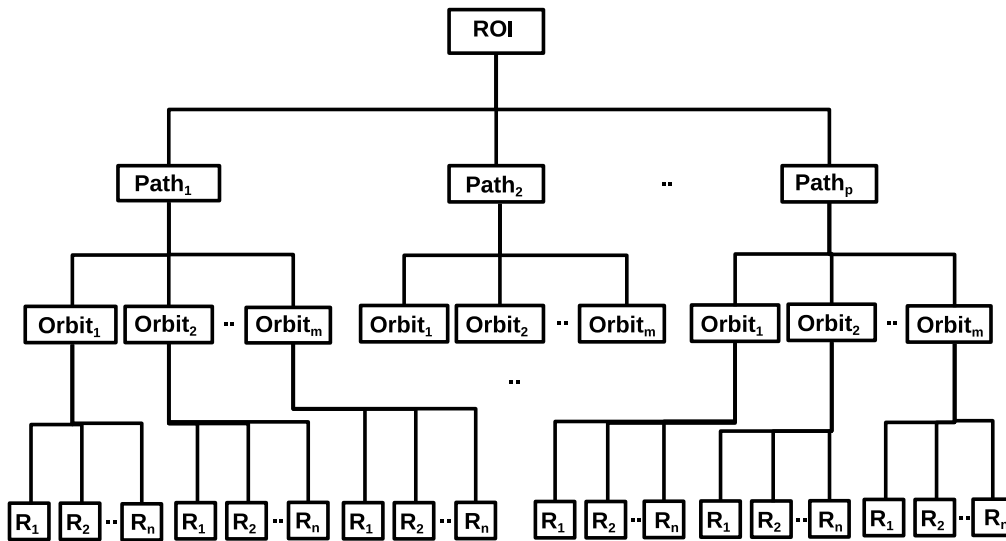


Fig. 2. A schematic representation of the input DEM scenes of a region of interest (ROI) using their metadata. A set of DEM scenes that belongs to a region of interest are represented as leaf nodes. This hierarchical structure provides the metadata for each DEM scene. A row from $\{R_i\}_{i=1}^n$ represents an individual DEM scene.

DEM scenes in the mosaic process is determined by the leaf nodes of the tree. This representation also identifies missing DEM scenes over a region of interest with the help of path-row referencing scheme. Our proposed framework presents a procedure to arrange the input DEM scenes based on their metadata using a vector data structure (Boyko, 2007), as described in Algorithm 1.

Algorithm 1: Metadata based hierarchical representation of the input DEM scenes.

```

Input : Input DEM scenes with metadata; a region of interest.
Output: DEM scenes (rows) segregated based on orbit-wise for each path.
1 Struct DEMInfo
   {
   string name; int path_num;
   int orbit_num; int row_num; }
   vector < DEMInfo > DEMInfo_roi;
   ▷ < DEMInfo_roi > is a vector that contains DEMInfo structures of all the DEM scene in a given region of interest.
   ▷ path is a vector of elements representing unique path numbers sorted in ascending order.
2 foreach path p in the path do
   foreach struct DEMInfo in < DEMInfo_roi > do
     ▷ UniOrbs stores unique orbit numbers of a given path
     if p = DEMInfo-> path_num then
       UniOrbs.push_back(DEMInfo-> orbit_num)
   foreach orbit orb in the vector < UniOrbs > do
     foreach struct DEMInfo in < DEMInfo_roi > do
       ▷ DEMnames stores file names of the DEMs for each orbit number of a given path
       if orb = DEMInfo-> orbit_num then
         DEMnames.push_back(DEMInfo-> name)
    
```

The structure *DEMInfo* represents the metadata of the DEM scenes as its elements. The vector $\langle DEMInfo_roi \rangle$ holds the meta data of the DEM scenes of an ROI. The *DEMnames* represents the rows of a path segregated based on the unique orbit numbers. The number of rows of a path typically varies based on the region of interest. Moreover, any two consecutive paths can have the DEM scenes (represented as rows) from two orbits of different seasons. Therefore, the cells in an overlapping region usually do not have same elevation values. The

nature of the feathering-based blend method itself does not consider more than two inputs at an instance. Hence, a selection mechanism is required, especially among the DEM scenes in the overlapping regions, during the mosaic process. Moreover, a random consideration of any two DEM scenes within an overlapping region is often a cause for the seams in the mosaic output, as described in Section 4.

3.2. Sequential ordering mechanism

The DEM scenes of same path with end-lap need not be acquired on the same day and DEM scenes with side-lap would be obviously acquired on different day. In either of the cases, the orbit numbers of acquired DEM scenes will be different. Clearly, the DEM scenes falling in the given ROI will have different orbit numbers even though they belong to the same path. The consequence of such DEM scenes result in elevation inconsistencies in the overlapping regions. A list is prepared with the orbit numbers of scenes falling in given ROI based on date and time of acquisition. The order in this list will not guarantee DEM scenes belonging to same path/same row i.e., they may be randomly placed in given ROI. This poses a demand to order by row and then by path.

Algorithm-2 explains a procedure to establish a sequence in which input DEM scenes are considered for mosaic process. This is helpful, especially when more than two DEM scenes exist in the overlapping regions within the ROI. DEM scenes belonging to a path number may possess different orbit numbers. DEM scenes with same orbit number of a path will undergo mosaic process using vertical blending method (α_v). The mosaic of rows (DEM scenes) for each orbit *i* of a path is denoted by *OrbitMosaic(i)*. The orbits of a path are considered to create path-wise DEM mosaic output using vertical blending. Finally, path-wise DEM mosaic outputs denoted by *PathMosaic(p)* for each path *p* are used to create a single seamless DEM using horizontal blending (α_h). *DEMmosaicFinal* represents the seamless DEM mosaic output for the given ROI.

The mosaic process employing feathering-based blending along with the order of precedence of the input DEM scenes is represented as

$$DEM_{mosaic} = f_h \left(\left\{ f_v \left(\left\{ f_v \left(\left\{ R_i^k(O_j) \right\}_{i=1}^n \right\}_{j=1}^m \right) \right) \right\}_{k=1}^p \right), \quad (1)$$

where $R_i^k(O_j)$ represents an input DEM scene that belongs to *i*th row of *j*th orbit in the path number *k*. The functions f_v and f_h represent

Algorithm 2: A traversal algorithm for sequential ordering of the input DEM scenes

Input : DEM scenes (rows) segregated based on orbit-wise for each path.
Output: A seamless mosaic of Input DEM scenes.
 ▷ *TotalPaths* denotes total number of paths

```

1 for  $p \leftarrow 1$  to TotalPaths do
  ▷ orbit(p) is a vector of elements representing unique orbits of the path number  $p$  sorted in ascending order.
  ▷ TotalOrbits denotes number of elements in orbit(p).
  for  $i \leftarrow 1$  to TotalOrbits do
    ▷ row is a vector of elements each represents an input DEM scene labeled with a row number available in an orbit(i). These elements are arranged in ascending order based on their row numbers.
    ▷ TotalRows denotes number of input DEM scenes available in an orbit(i).
    for  $j \leftarrow 1$  to TotalRows do
      if  $j > 1$  then
        |  $RowMosaic(j) \leftarrow RowMosaic(j-1)(\alpha_v)row(j)$ 
      else
        |  $RowMosaic(j) \leftarrow row(j)$ 
       $RowMosaicFinal \leftarrow RowMosaic(j)$ 
      if  $i > 1$  then
        |  $OrbitMosaic(i) \leftarrow$ 
        |  $OrbitMosaic(i-1)(\alpha_v)RowMosaicFinal$ 
      else
        |  $OrbitMosaic(i) \leftarrow RowMosaicFinal$ 
     $OrbitMosaicFinal \leftarrow OrbitMosaic(i)$ 
  if  $p > 1$  then
    |  $PathMosaic(p) \leftarrow PathMosaic(p-1)(\alpha_h)OrbitMosaicFinal$ 
  else
    |  $PathMosaic(p) \leftarrow OrbitMosaicFinal$ 
 $DEM Mosaic \leftarrow PathMosaic(p)$ 

```

vertical and horizontal blending which are defined in Eqs. (2), and (3), respectively. These are explained in detail in Section 3.3.

$$f_v(E_1, E_2, \dots, E_n) = \alpha_v \left(\alpha_v (\alpha_v (E_1, E_2), E_3), \dots, E_n \right) \quad (2)$$

$$f_h(S_1, S_2, \dots, S_n) = \alpha_h \left(\alpha_h (\alpha_h (S_1, S_2), S_3), \dots, S_n \right) \quad (3)$$

where $\{E_k\}_{k=1}^n$ and $\{S_k\}_{k=1}^n$ represent end-lap and side-lap DEMs, respectively.

The expression trees shown in Fig. 3 provide an abstract view of the order of precedence in DEM mosaic process. The construction of expression trees for all the orbits available within a path number will have to be carried out in the same way as shown in Fig. 3(a–c). The Expression tree shown in Fig. 3(d) must be replicated for each path number involved in the region of interest. Finally, Fig. 3(e) represents the mosaic of all the available paths and generates a single seamless DEM for the defined region of interest. In general, the rows of a path are from different orbits.

3.3. Two variants of blending

This section explains a methodology to address the factors that affect the overlapping regions during mosaic process. It is common to have multiple overlapping regions, each with more than two DEM scenes. The input DEM scenes of Cartosat-1 are indicated based on the path-rows of their corresponding stereo pairs. All the corrected input

DEM scenes of a region of interest are considered for mosaic process. These are identified using point-in-polygon method (Harrington, 1983). Here, the region of interest is considered as a polygon and each corner of the individual DEM scene is considered iteratively as a point. An input DEM scene belongs to the region of interest, if any one of its points lies in the polygon.

Our framework includes two variants of the feathering-based blend method, namely, vertical and horizontal blend methods during the mosaic process. These are used to handle various possible cases of DEM overlaps. These are categorized based on the containment relation between two input DEM scenes in the overlapping region. Each method has its own mechanism to derive the weights for the distance-weighted algorithm.

3.3.1. Vertical blending (α_v)

Vertical blending is used to process the end-lap DEM scenes. Fig. 4(a) shows a case of two DEMs $R_1^1(O_1)$ and $R_2^1(O_1)$ with overlap, where $R_1^1(O_1)$ and $R_2^1(O_1)$ represent the input DEM scenes that belong to row number 1 and row number 2 from orbit number 1 in path number 1, respectively. Every cell in the overlapping region PQRS, as shown in Fig. 4(b), contains two elevation values. For example, the cell marked with X in Fig. 4(b) has values from the two DEM scenes, $R_1^1(O_1)$ and $R_2^1(O_1)$. Since X is closer to the DEM scene $R_1^1(O_1)$, the elevation value of $R_1^1(O_1)$ at X is assigned more weight during the blending process. In this method, the weights are derived for each column of the overlapping region PQRS separately.

The weight of i th cell in a j th column is derived as

$$W_{v(i,j)} = (T_j - i)/(T_j - 1), \quad (4)$$

where T_j represents the number of cells in j th column. The value of $W_{v(i,j)}$ represents the weight derived for i th cell in j th column. Upon weight derivation of each cell in the overlapping region using Eq. (4), the vertical blending (α_v) is performed using

$$\alpha_v(R_1^1(O_1), R_2^1(O_1)) = R_1^1(O_1) \times W_v + R_2^1(O_1) \times (1 - W_v), \quad (5)$$

where W_v represents weights of the cells in the overlapping region between the end-lap DEM scenes $R_1^1(O_1)$ and $R_2^1(O_1)$.

3.3.2. Horizontal blending (α_h)

Horizontal blending is used to process the side-lap DEM scenes. Fig. 5(a) shows a case of two DEMs $R_1^1(O_1)$ and $R_1^2(O_2)$, where $R_1^1(O_1)$ and $R_1^2(O_2)$ represent the input DEM scenes that belong to row number 1 from different orbits and paths, respectively. Every cell in the overlapping region $P'Q'R'S'$, as shown in Fig. 5(b), contains two elevation values. For example, the cell marked with Y in Fig. 5(b) has values from the two DEM scenes, $R_1^1(O_1)$ and $R_1^2(O_2)$. Since the Y is closer to the DEM scene $R_1^1(O_1)$, the cell of the $R_1^1(O_1)$ is assigned more weight during the blending process. In this method, the weights are derived for each column of the overlapping region $P'Q'R'S'$ separately.

The weight of j th cell in a i th row is derived as

$$W_{h(i,j)} = (T_i - j)/(T_i - 1), \quad (6)$$

where T_i represents the number of cells in i th row. The value of $W_{h(i,j)}$ represents the weight derived for j th cell in i th row. Upon weight derivation of each cell in the overlapping region using Eq. (6), the horizontal blending (α_h) is performed using

$$\alpha_h(R_1^1(O_1), R_1^2(O_2)) = R_1^1(O_1) \times W_h + R_1^2(O_2) \times (1 - W_h), \quad (7)$$

where W_h represents weights of the cells in the overlapping region between the side-lap DEM scenes $R_1^1(O_1)$ and $R_1^2(O_2)$. However, the elevation values of the cells outside the overlapping region are not weighted as they do not participate in the blending process.

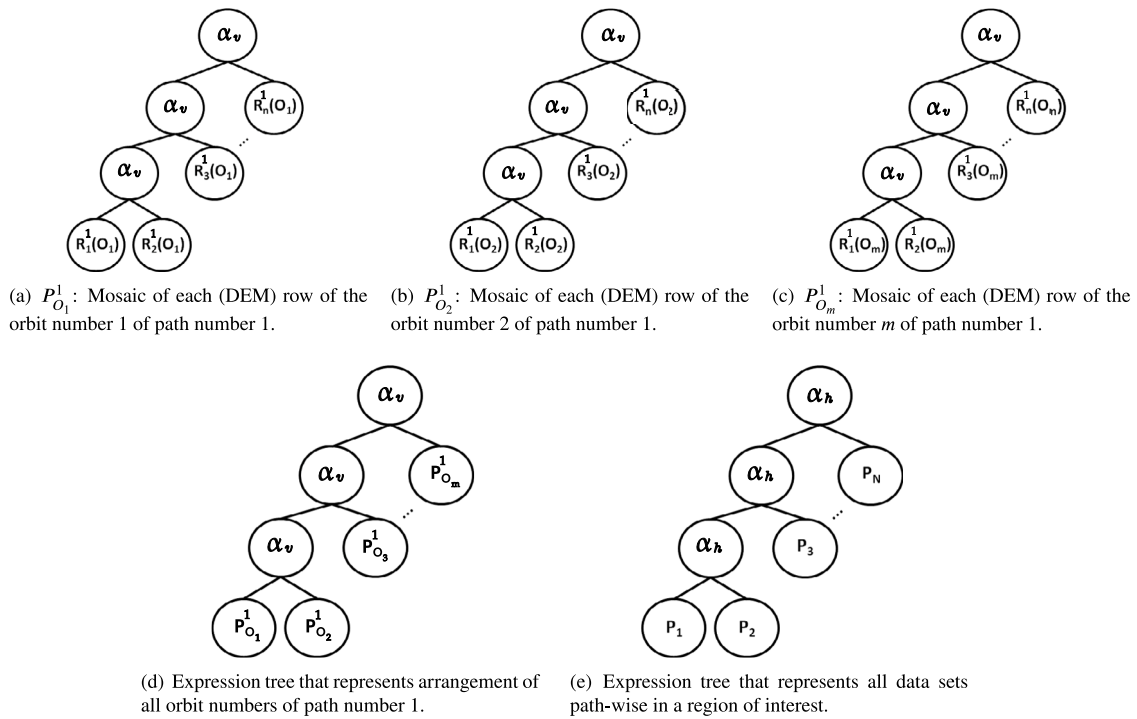


Fig. 3. The expression trees representing the sequence of mosaic process. The nodes in an expression tree are traversed using post order traversal. Each internal node including root represents an operator. Here, the operators, α_h and α_v , define the variant of blending method (explained in detail in Section 3.3) between two DEM scenes.

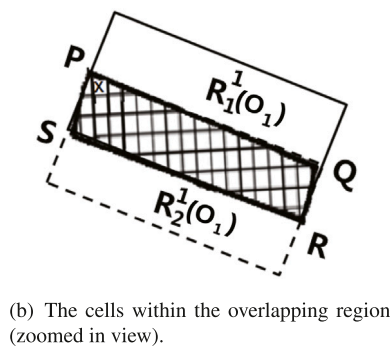
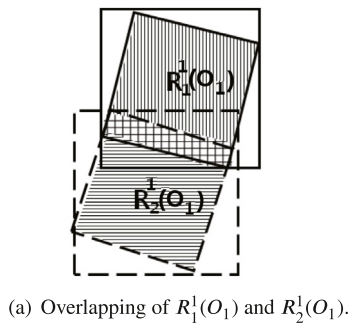


Fig. 4. A typical scenario of the vertical feathering-based blend method. A cell is marked with X in the overlapping region PQRS. Each cell in this overlapping region has two elevation values. The mosaic process considers elevation values along each vertical direction in PQRS.

4. Experiments and evaluation

This section presents the experimental setup, the study area, and a comparison of mosaic methods such as the average method and the conventional feathering-based blend method with the proposed method.

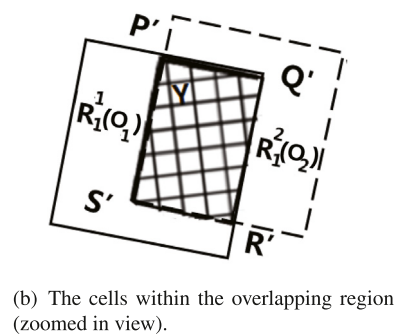
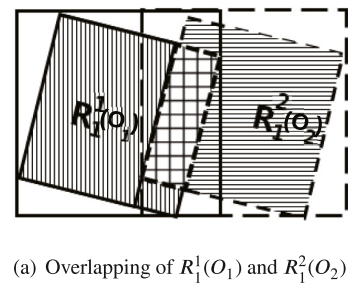


Fig. 5. A typical scenario of the horizontal feathering-based blend method. A cell is marked with Y in the overlapping region $P'Q'R'S'$. Each cell in this overlapping region has two elevation values. The mosaic process considers the elevation values along each horizontal direction in $P'Q'R'S'$.

These three mosaic methods are implemented in C++. The experiments are conducted on a computer system that has 2-Intel Xeon processors with 12 cores each, 16 GB main memory. We generate and compare the DEM mosaic outputs over the same study area. We also analyze the elevation profiles of the mosaic output of the proposed method. The following subsections provide the details of the experimentation.

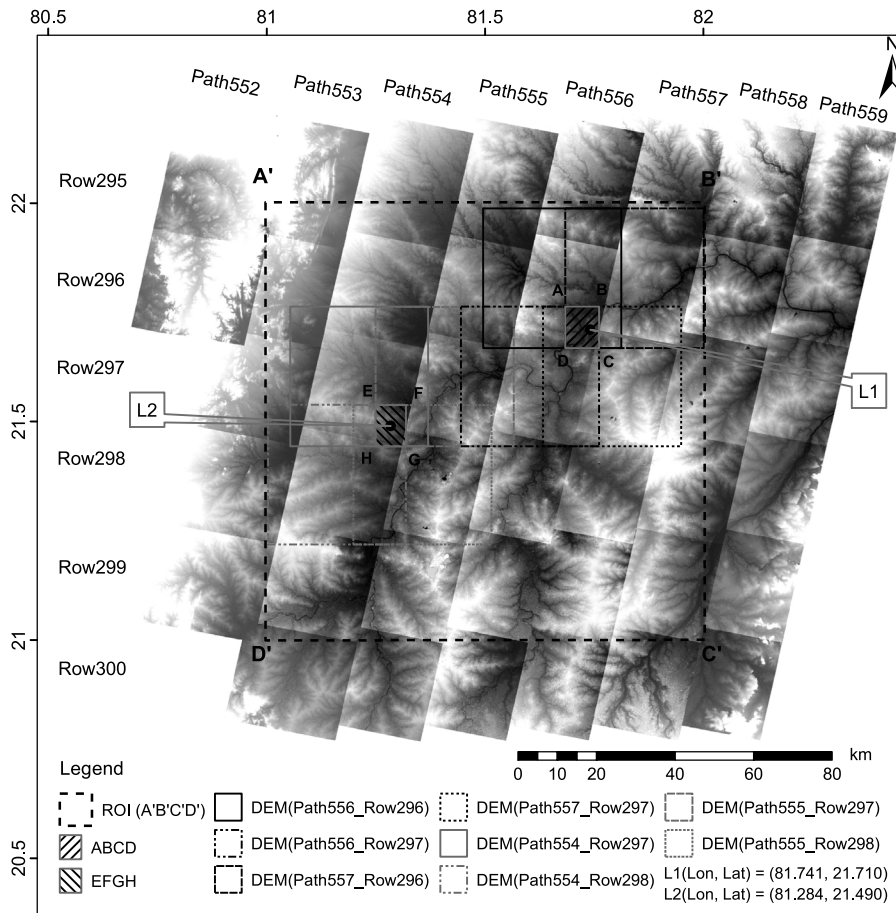


Fig. 6. A glimpse of Cartosat-1 input DEM scenes for the ROI A'B'C'D'. The overlapping regions ABCD and EFGH are considered for the evaluation.

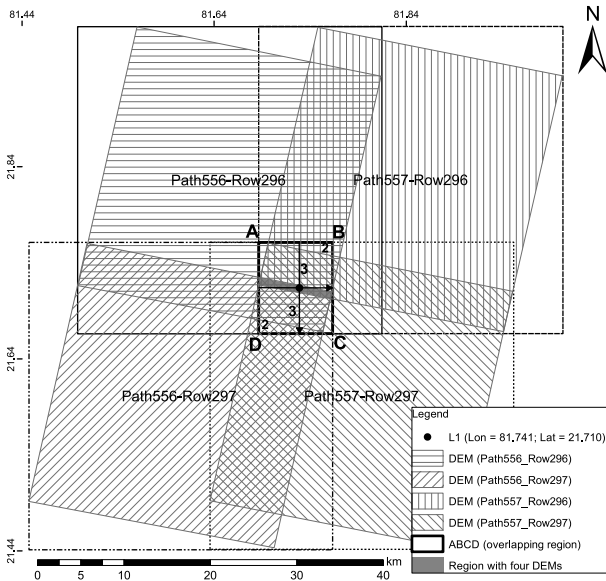


Fig. 7. Overlapping region ABCD. A small area filled with grey color represents the intersection of the four DEM scenes. Each cell in this grey region has four elevation values. Arrows indicate the direction in which the elevations of the cells considered to generate the profiles.

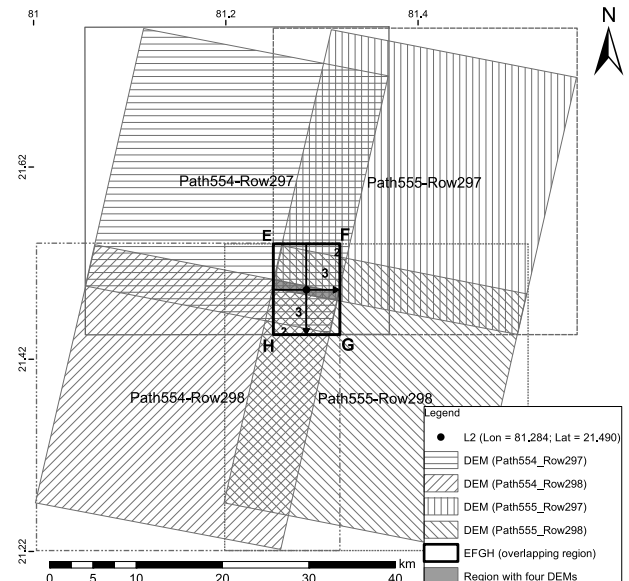


Fig. 8. Overlapping region EFGH. A small area filled with grey color represents the intersection of the four DEM scenes. Each cell in this grey region has four elevation values. Arrows indicate the direction in which the elevations of the cells considered to generate the profiles.

4.1. Study area

The Cartosat-1 DEM scenes with 10 m posting are considered to create a mosaic for a region of $1^\circ \times 1^\circ$. Each DEM scene has the planimetric and vertical accuracies of 15 m and 8 m, respectively (Giribabu et al., 2013). We consider an ROI that covers $110 \times 110 \text{ km}^2$, a part of Chhattisgarh region in India, extending $1^\circ \times 1^\circ$ from 21°N latitude and 81°E longitude. The ROI denoted by $A'B'C'D'$ as shown in Fig. 6, includes 40 Cartosat-1 individual DEM scenes and each scene covers approximately $27.5 \text{ km} \times 27.5 \text{ km}$ area.

We consider two overlapping regions within $A'B'C'D'$, namely, $ABCD$ and $EFGH$ as shown in Fig. 6 for the evaluation. $ABCD$ contains several drainage patterns with a river segment. Furthermore, $ABCD$ is relatively an undulating terrain to $EFGH$, though their elevation ranges are nearly the same. The first region $ABCD$ represents an overlapping region with the extents of $top = 21.763234$; $bottom = 21.668172$; $left = 81.683696$; $right = 81.760694$ in decimal degrees covering approximately 84 km^2 . The region $ABCD$ contains four individual DEM scenes, namely, rows 296 and 297 of path 556, rows 296 and 297 of path 557. Other region $EFGH$ represents an overlapping region with the extents of $top = 21.537789$; $bottom = 21.443390$; $left = 81.249553$; $right = 81.318776$ in decimal degrees covering approximately 75 km^2 . The region $EFGH$ contains four individual DEM scenes, namely, rows 297 and 298 of path 554, rows 297 and 298 of path 555.

4.2. DEM mosaic methods

This section describes the average method, the feathering-based blend method, and the proposed method over the two overlapping regions $ABCD$ and $EFGH$ as shown in Figs. 7 and 8, respectively. Each overlapping region partially involve four DEM scenes, two rows from two different paths. A cell in an overlapping region has multiple elevation values that vary from one to four. The average method simply computes the mean of the elevation values of a cell. Where as, the feathering-based blend method transforms the elevation values of a cell iteratively with weights derived based on its position in the corresponding two input DEM scenes in an instance. Hence, the output of feathering-based blend method depends on the sequence with which inputs are considered during mosaic process. The proposed method determines a unique sequence of the inputs based on the metadata, which is subsequently used in the feathering-based blend method. Here, the comparison of these methods exhibits the essence of the sequential ordering mechanism in manifesting the seamless mosaic. The following subsections illustrate these three mosaic methods over the overlapping regions $ABCD$ and $EFGH$.

4.2.1. Average method

The average method computes the mean of the elevation values available for each cell in an overlapping region. Though the average method can be performed in a single instance, it is described in three steps to have a better comparison with the subsequent methods. The sequence of steps in the average method does not alter the mosaic output. The following three steps are involved in the mosaic process using the average method over the region $ABCD$.

$$L_{step1} = \text{Average}\left(R_{296}^{556}(O_{8536}), R_{297}^{556}(O_{8536})\right) \quad (8)$$

$$L_{step2} = \text{Average}\left(R_{296}^{557}(O_{10240}), R_{297}^{557}(O_{10240})\right) \quad (9)$$

$$L_{step3} = \text{Average}\left(L_{step1}, L_{step2}\right) \quad (10)$$

The L_{step1} determines the average value of the DEM scenes representing the row numbers 296 and 297 of the orbit number 8536. The L_{step2} determines the average value of the DEM scenes representing the row numbers 296 and 297 of the orbit number 10240. The L_{step3} considers the outputs of the steps L_{step1} and L_{step2} and determines the average of the elevation values in the overlapping region. Similarly,

the following three steps are involved in the mosaic process using the average method over the region $EFGH$.

$$L'_{step1} = \text{Average}\left(R_{297}^{554}(O_{8862}), R_{298}^{554}(O_{8862})\right) \quad (11)$$

$$L'_{step2} = \text{Average}\left(R_{297}^{555}(O_{8699}), R_{298}^{555}(O_{8699})\right) \quad (12)$$

$$L'_{step3} = \text{Average}\left(L'_{step1}, L'_{step2}\right) \quad (13)$$

4.2.2. Feathering-based blend method

The feathering-based blend method adjusts the cell values in the overlapping region using distance-based weight algorithm. Following three steps are involved in the mosaic process using this method confined to the region $ABCD$.

$$M_{step1} = \alpha_v\left(R_{296}^{556}(O_{8536}), R_{297}^{556}(O_{8536})\right) \quad (14)$$

$$M_{step2} = \alpha_h\left(M_{step1}, R_{296}^{557}(O_{10240})\right) \quad (15)$$

$$M_{step3} = \alpha_h\left(M_{step2}, R_{297}^{557}(O_{10240})\right) \quad (16)$$

The M_{step1} is the output of the vertical feathering-based blend method between the DEM scenes representing the row numbers 296 and 297 of the same orbit number 8536. The output from the M_{step1} and the DEM scene representing row number 296 from the orbit number 10240 undergoes horizontal feathering-based blend method in the M_{step1} . Finally, the output from the M_{step2} and the DEM scene representing row number 297 from the orbit number 10240 undergoes horizontal feathering-based blend method in the M_{step3} . Similarly, the following three steps are involved in the mosaic process using the feathering-based blend method over the region $EFGH$.

$$M'_{step1} = \alpha_v\left(R_{297}^{554}(O_{8862}), R_{298}^{554}(O_{8862})\right) \quad (17)$$

$$M'_{step2} = \alpha_h\left(M'_{step1}, R_{297}^{555}(O_{8699})\right) \quad (18)$$

$$M'_{step3} = \alpha_h\left(M'_{step2}, R_{298}^{555}(O_{8699})\right) \quad (19)$$

4.2.3. The proposed method

The proposed method determines the variant of the feathering-based blend method in conjunction with the unique sequence during the mosaic process. The following three steps are constructed based on the sequence to perform mosaic over the region $ABCD$.

$$N_{step1} = \alpha_v\left(R_{296}^{556}(O_{8536}), R_{297}^{556}(O_{8536})\right) \quad (20)$$

$$N_{step2} = \alpha_v\left(R_{296}^{557}(O_{10240}), R_{297}^{557}(O_{10240})\right) \quad (21)$$

$$N_{step3} = \alpha_h\left(N_{step1}, N_{step2}\right) \quad (22)$$

The N_{step1} is the output of the vertical feathering-based blend method between the DEM scenes representing the row numbers 296 and 297 of the same orbit number 8536. The N_{step2} performs vertical feathering-based blend method between the DEM scenes belong to row numbers 296 and 297 of the same orbit number 10240. The outputs from the N_{step1} and N_{step2} are considered for horizontal feathering-based blend method. Similarly, the following three steps are constructed based on the sequence to perform mosaic over the region $EFGH$.

$$N'_{step1} = \alpha_v\left(R_{297}^{554}(O_{8862}), R_{298}^{554}(O_{8862})\right) \quad (23)$$

$$N'_{step2} = \alpha_v\left(R_{297}^{555}(O_{8699}), R_{298}^{555}(O_{8699})\right) \quad (24)$$

$$N'_{step3} = \alpha_h\left(N'_{step1}, N'_{step2}\right) \quad (25)$$

The key difference between the proposed method and the conventional feathering-based blend method is the ordering of input DEM scenes during the mosaic process. In the proposed method, the vertical blending is performed over the input DEM scenes of each path separately. And, then horizontal blending is performed over the obtained path-wise mosaic outputs to create a seamless DEM mosaic.

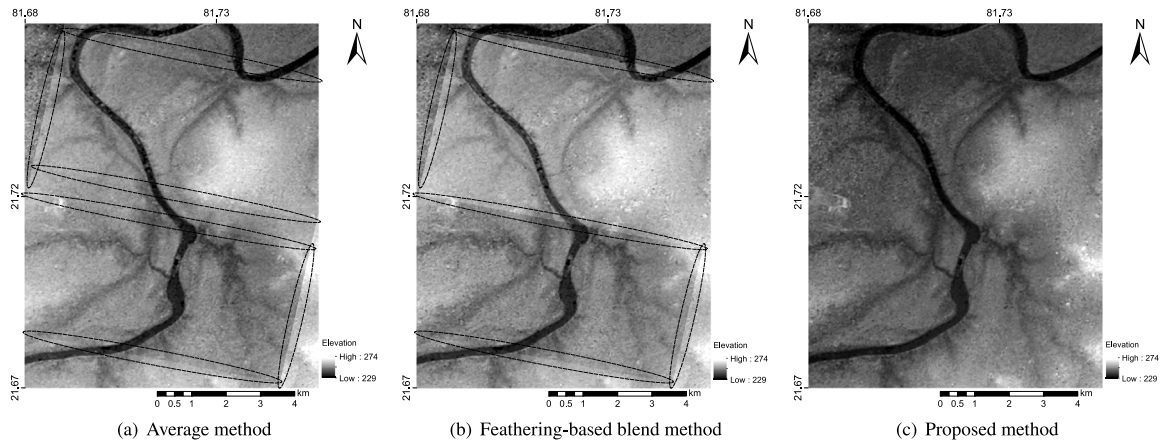


Fig. 9. Cartosat-1 DEM mosaic outputs over the overlapping region *ABCD* using average method, feathering-based blend method, and the proposed method. The seams present in Fig. 9(a) and (b) are marked with ellipses. The seamless mosaic is shown in Fig. 9(c).

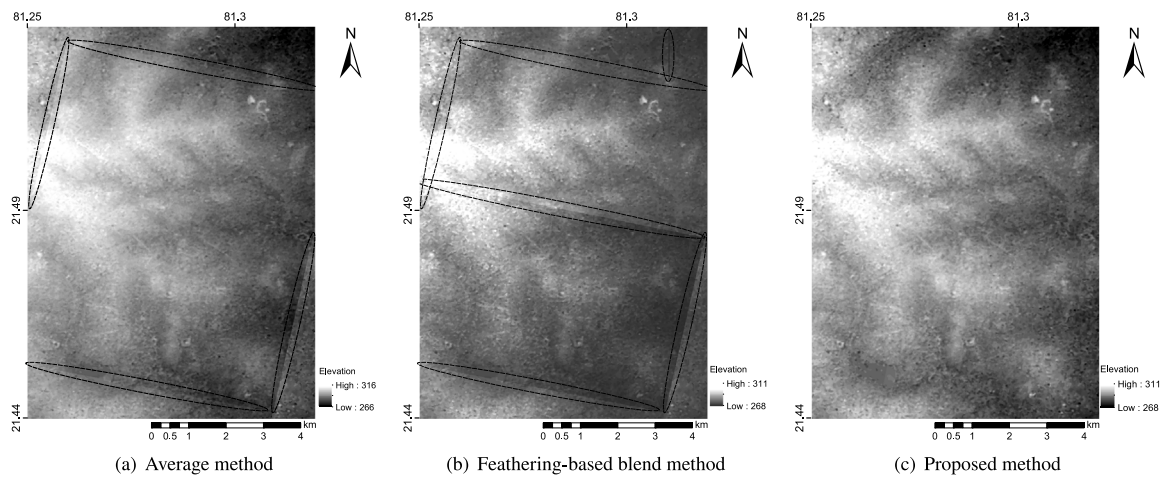


Fig. 10. Cartosat-1 DEM mosaic outputs over the overlapping region *EFGH* using average method, feathering-based blend method, and the proposed method. The seams present in Fig. 10(a) and (b) are marked with circles. The seamless mosaic is shown in Fig. 10(c).

4.3. Experimental results

In this section, we discuss the experimental results and evaluation of the proposed method. We show the Cartosat-1 DEM mosaic outputs for the region *A'B'C'D'* and its two overlapping regions *ABCD* and *EFGH*. A quantitative analysis on these mosaic outputs using elevation profiles, relative elevation consistency, and mean terrain ruggedness index, is also presented in the subsequent sections.

4.3.1. Cartosat-1 DEM mosaic outputs

Figs. 9 and 10 show the DEM mosaic outputs using three methods for the overlapping regions *ABCD* and *EFGH*, respectively. It is apparent from the results that the average method and feathering-based blend method, without a suitable ordering of scenes, introduce the seams along the borders of the input DEM scenes in the overlapping regions *ABCD* and *EFGH*. The proposed method, which determines an unique input sequence exhibits seamless transition of the elevation values within the overlapping regions.

The DEM mosaic outputs obtained from these three mosaic methods along with their hill-shades for the ROI *A'B'C'D'* are shown in Figs. 11 to 13, respectively. The run-time of average, feathering-based blend, and the proposed methods for a region of $1^\circ \times 1^\circ$ (approximately 12 100 km²) is 2.1, 1.8, and 1.7 min, respectively.

The proposed method exhibits a smooth elevation transition in the overlapping regions of the mosaic outputs. The other two methods

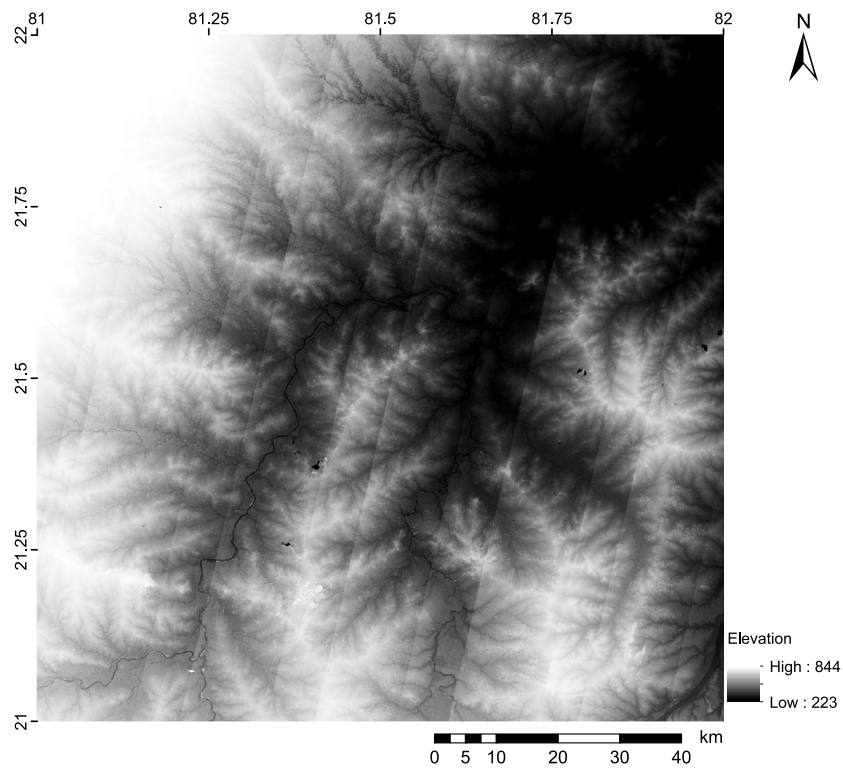
exhibit the presence of seam lines in the mosaic outputs as shown clearly in Figs. 9 to 13. The weights derivation mechanism and the ordering of input DEM scenes followed in these two methods may have influenced the presence of seams.

4.3.2. Elevation profiles

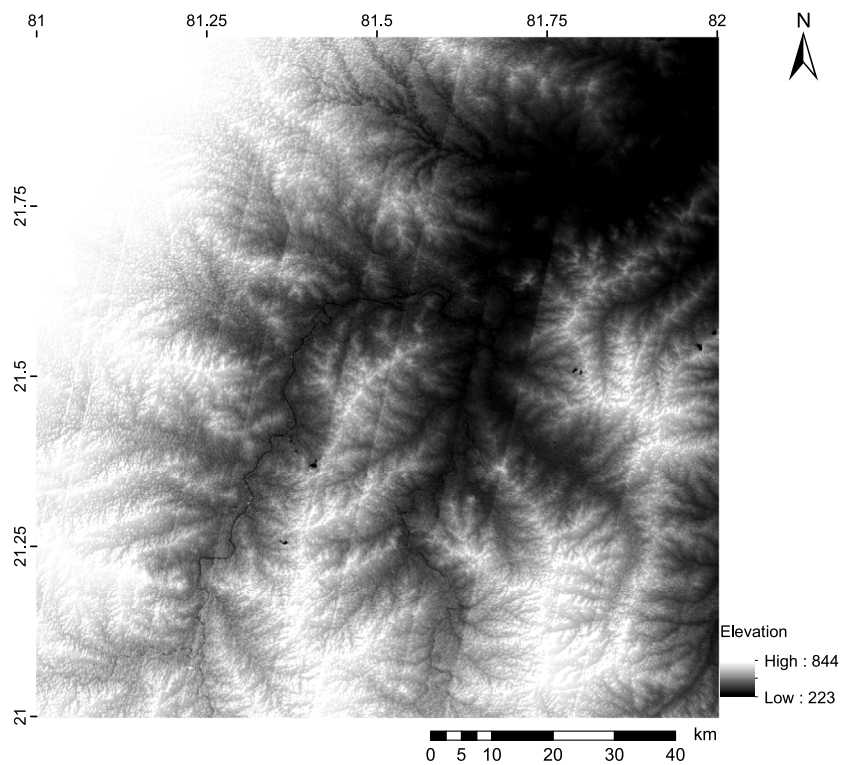
We consider the locations *L1* and *L2* of the overlapping regions *ABCD* and *EFGH*, as indicated in Figs. 7 and 8, respectively, to study the elevation profiles of three mosaic methods. Each overlapping region has multiple subregions vary from one to four. These subregions of *ABCD*, *EFGH* are denoted by the number of input DEM scenes containing elevation data as shown in Figs. 7 and 8, respectively. The subregions of an overlapping region with more than two DEM scenes undergo mosaic process with both vertical and horizontal feathering-based blending. Hence, both horizontal and vertical profiles are considered for the analysis. These elevation profiles are segmented into subregions based on the number of DEM scenes participated in mosaic process. The number of subregions and their extents also may vary across the profiles.

ABCD region

Fig. 14 shows both horizontal and vertical elevation profiles over the location *L1* within the overlapping region *ABCD*. The horizontal and vertical profiles are generated along the lines passing 7.96 km horizontally and 10.56 km vertically through the location *L1*, respectively.



(a) Average method

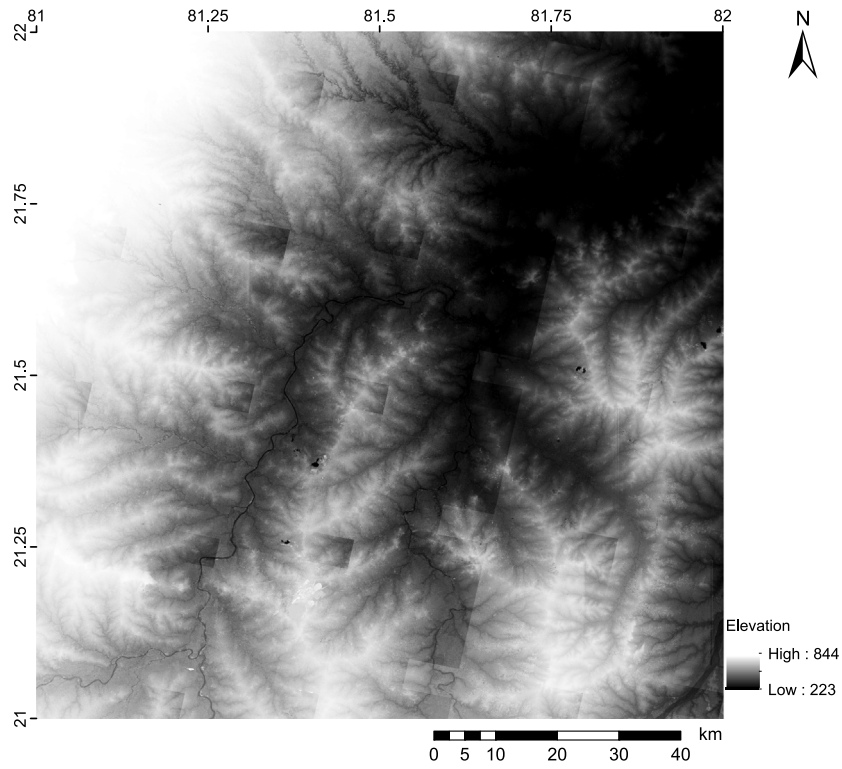


(b) Hill-shade of Figure 11(a)

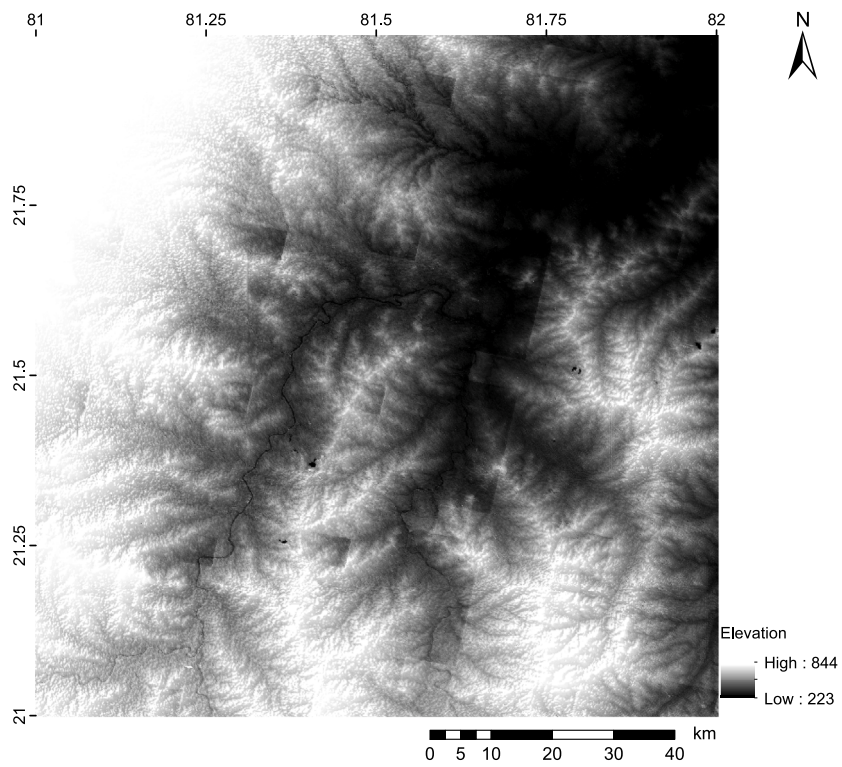
Fig. 11. Cartosat-1 DEM mosaic using average method for the region $A'B'C'D'$ (indicated in Fig. 6). The elevation discrepancies are apparently visible across the paths.

The horizontal elevation profile is segmented into three subregions as shown in Fig. 14. The *subregion1* considers the elevation values from only three DEM scenes. It excludes Path557-Row296 DEM, as

it contains *NODATA*. The *subregion2* considers elevation values from all the four DEM scenes. Similarly, the *subregion3* considers elevation values from three DEM scenes and excludes Path556-Row297 DEM, as

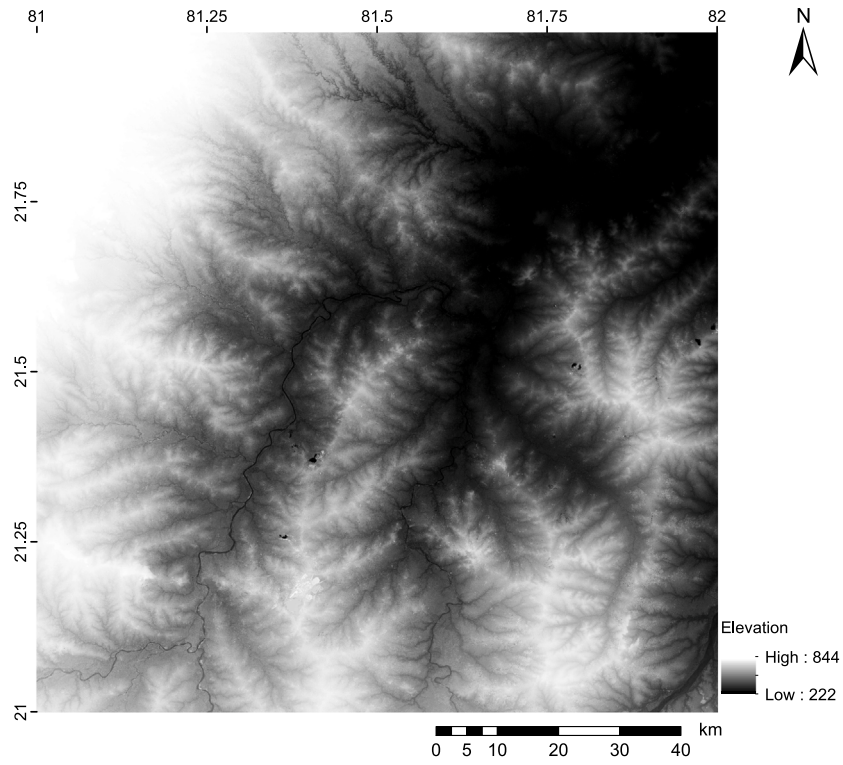


(a) Feathering-based blend method

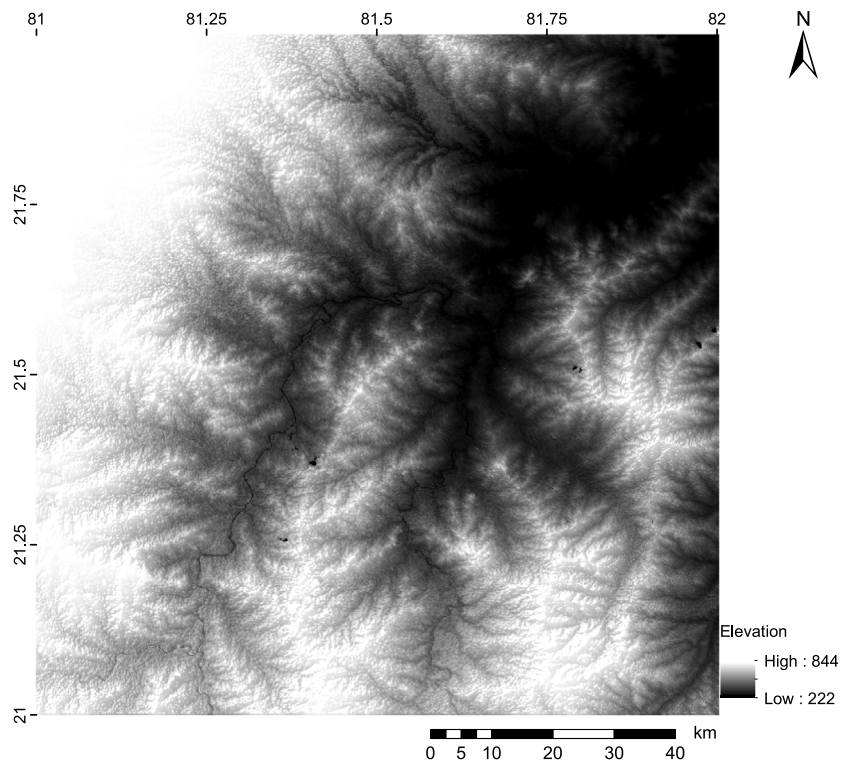


(b) Hill-shade of Figure 12(a)

Fig. 12. Cartosat-1 DEM mosaic using feathering-based blend method for the region $A'B'C'D'$ (indicated in Fig. 6). The elevation discrepancies are apparently visible across the paths.

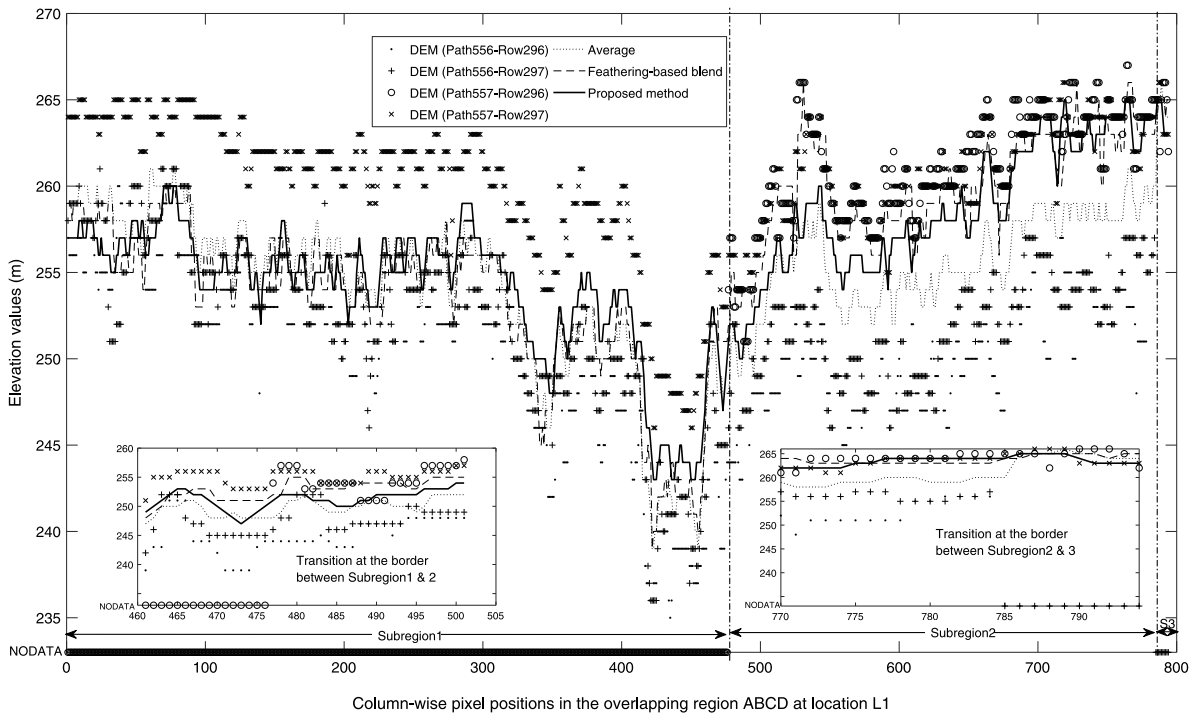


(a) Proposed method

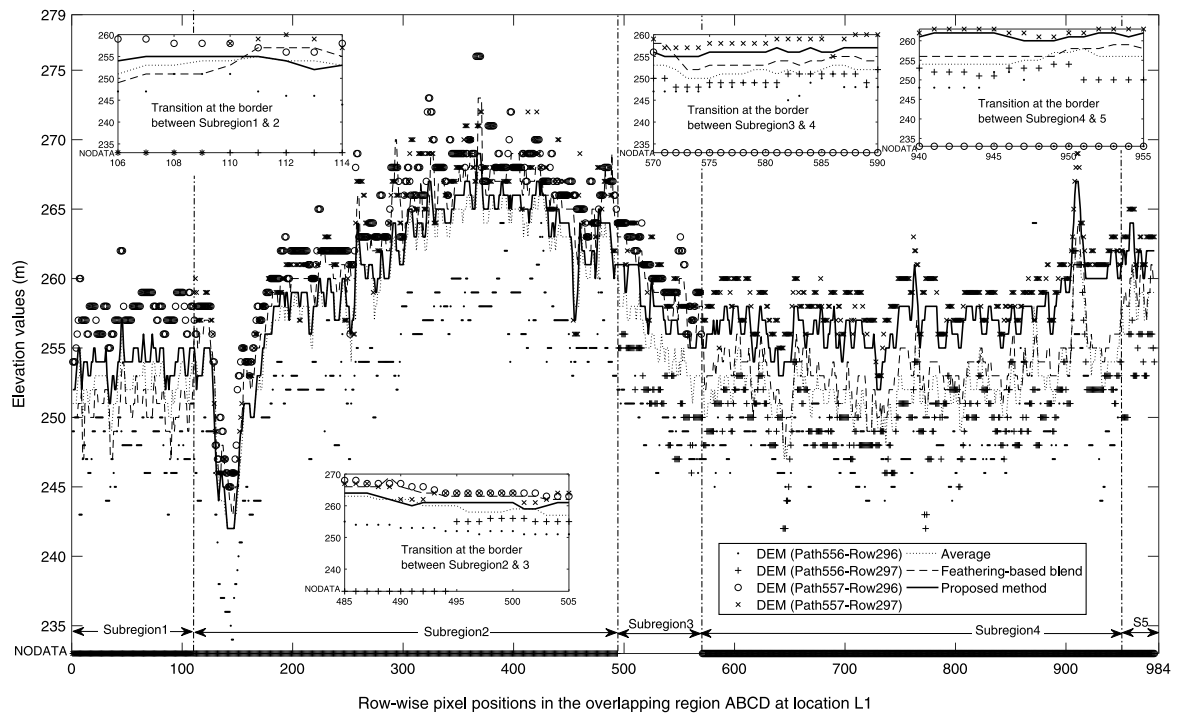


(b) Hill-shade of Figure 13(a)

Fig. 13. Cartosat-1 DEM mosaic using the proposed method for the region $A'B'C'D'$ (indicated in Fig. 6). The propose framework exhibits the seamless transition in the overlapping regions.



(a) Horizontal profiles at the location *L1* in the overlapping region *ABCD*.



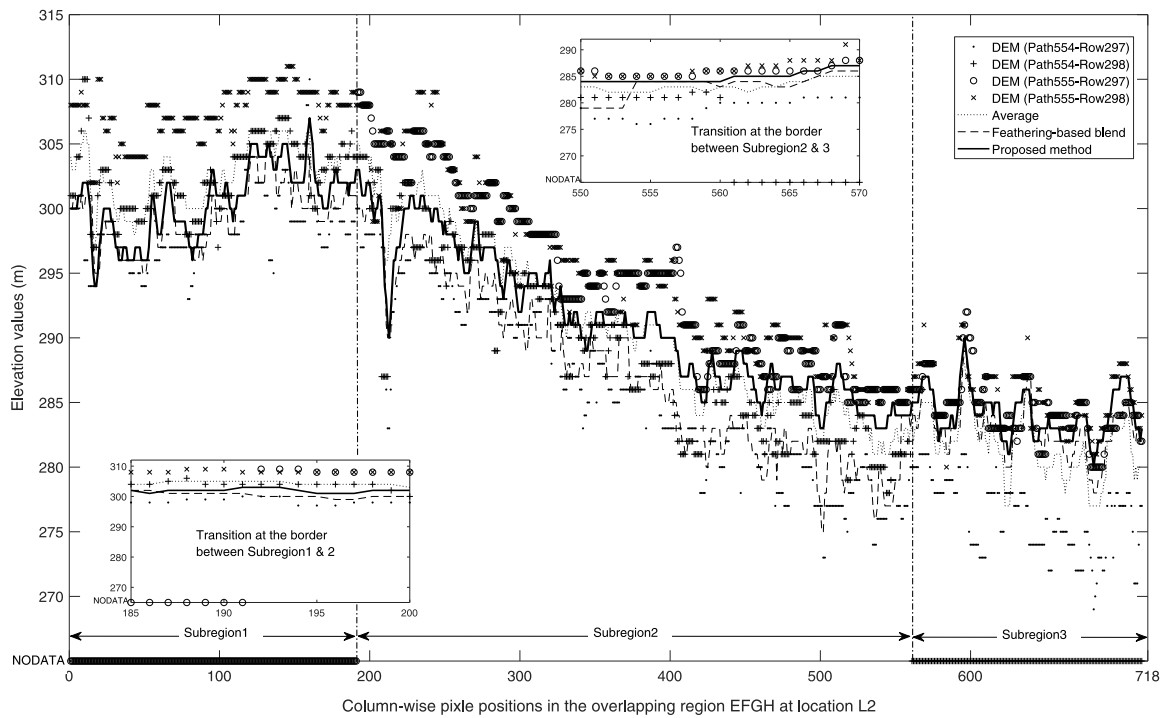
(b) Vertical profiles of the three mosaic methods over the location *L1* in the overlapping region *ABCD*.

Fig. 14. Elevation profiles of the mosaic outputs obtained from the three mosaic methods and the DEM scenes involved along the line passing horizontally and vertically through the location *L1*. A smooth elevation transition between the subregions are observed.

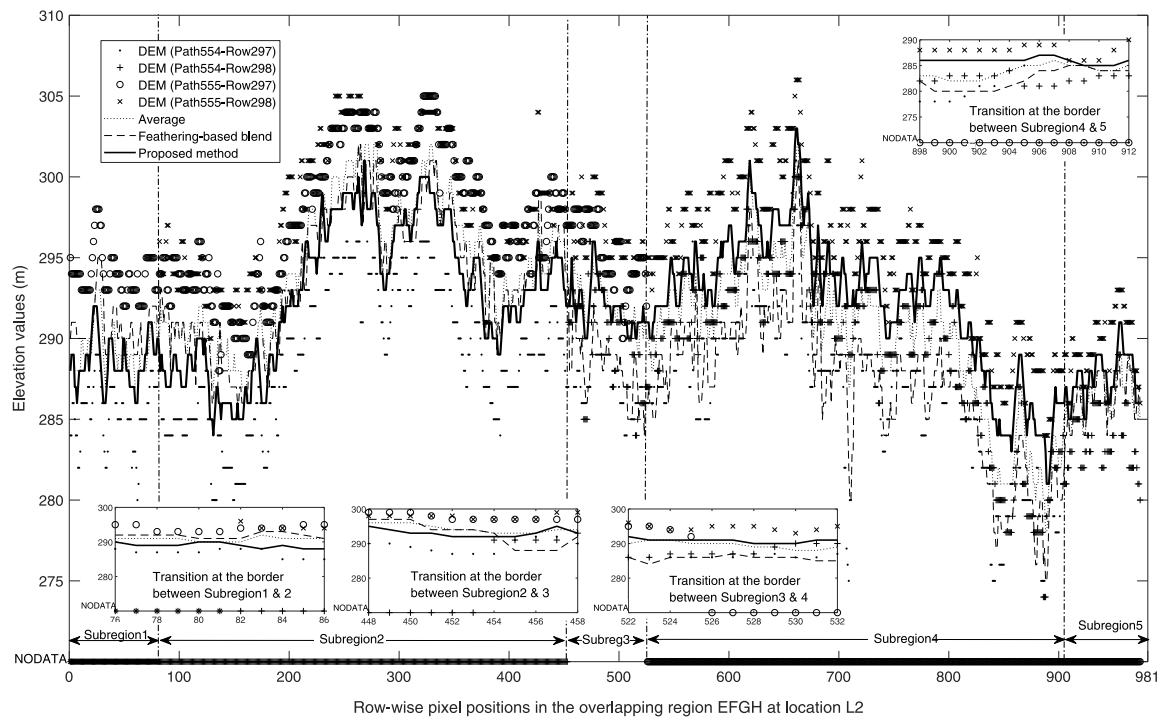
it contains *NODATA*. The proposed method exhibits a smooth handover of the elevation values horizontally between the subregions while preserving the elevation values within their input range.

The vertical elevation profile is segmented into five subregions as shown in Fig. 14. The *subregion1* considers the elevation values

from only two DEM scenes. It excludes Path556-Row297 and Path557-Row297 DEM scenes, as they contain *NODATA*. The *subregion2* considers elevation values from three DEM scenes and excludes Path556-Row297 DEM, as it contains *NODATA*. The *subregion3* considers elevation values from all the four DEM scenes. The *subregion4* considers



(a) Horizontal profiles at the location $L2$ in the overlapping region $EFGH$.



(b) Vertical profiles of the three mosaic methods over the location $L2$ in the overlapping region $EFGH$.

Fig. 15. Elevation profiles of the mosaic outputs obtained from the three mosaic methods and the DEM scenes involved along the line passing horizontally and vertically through the location $L2$. A smooth elevation transition between the subregions are observed.

elevation values from three DEM scenes and excludes Path557-Row296 DEM, as it contains *NODATA*. The *subregion5* considers the elevation values from only two DEM scenes. It excludes Path556-Row296 and Path557-Row296 DEM scenes, as they contain *NODATA*. The proposed

method also exhibits a smooth handover of the elevation values vertically between the subregions while preserving the elevation values within their input range. The weights of both vertical and horizontal blend methods ensure a seamless elevation transition between the rows of the path and across the paths, respectively.

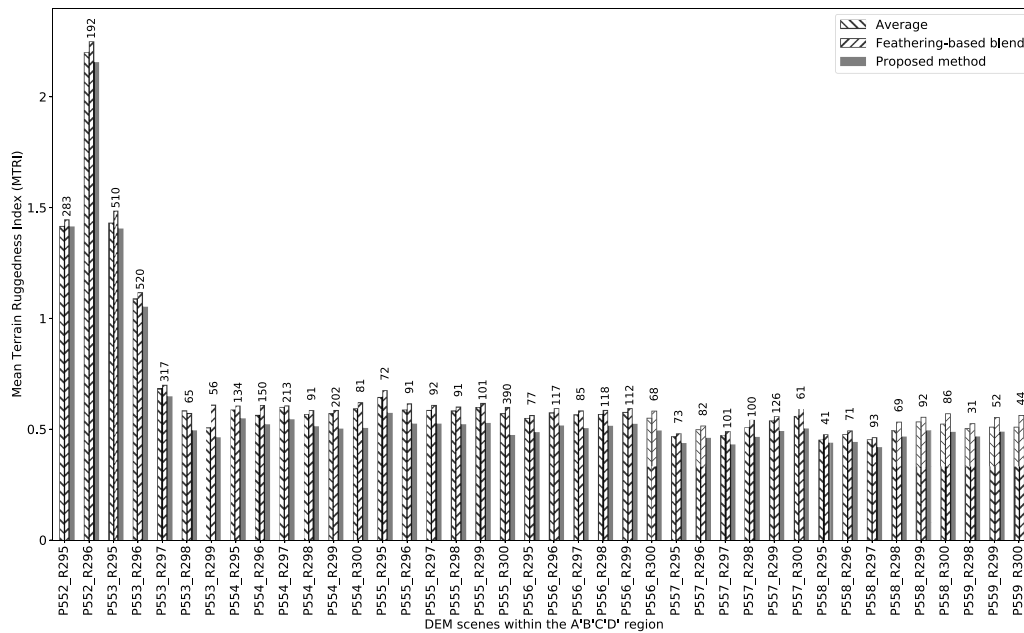


Fig. 16. Mean terrain ruggedness index of the Cartosat-1 DEM mosaic outputs from the average, feathering-based blend, and proposed method confining to each input DEM scene within A'B'C'D' region. The numerical value on top of each bar represents elevation range of the corresponding input DEM scene.

EFGH region

Fig. 15 shows both horizontal and vertical profiles over the location L2 within the overlapping region EFGH. The horizontal and vertical profiles are generated along the lines passing 7.17 km horizontally and 10.45 km vertically through the location L2, respectively.

The horizontal elevation profile of EFGH is segmented into three subregions as shown in Fig. 15. The subregion1 considers the elevation values from only three DEM scenes. It excludes Path555-Row297 DEM, as it contains NODATA. The subregion2 considers elevation values from all the four DEM scenes. Similarly, the subregion3 considers elevation values from three DEM scenes and excludes Path554-Row298 DEM, as it contains NODATA. The proposed method exhibits a smooth handover of the elevation values horizontally between the subregions while preserving the elevation values within their input range.

The vertical elevation profile is segmented into five subregions as shown in Fig. 15. The subregion1 considers the elevation values from only two DEM scenes. It excludes Path554-Row298 and Path555-Row298 DEM scenes, as they contain NODATA. The subregion2 considers elevation values from three DEM scenes and excludes Path554-Row298 DEM, as it contains NODATA. The subregion3 considers elevation values from all the four DEM scenes. The subregion4 considers elevation values from three DEM scenes and excludes Path555-Row297 DEM, as it contains NODATA. The subregion5 considers the elevation values from only two DEM scenes. It excludes Path554-Row297 and Path555-Row297 DEM scenes, as they contain NODATA. The proposed method also exhibits a smooth handover of the elevation values vertically between the subregions while preserving the elevation values within their input range. It is noteworthy that the source of elevations in the subregions changes within the overlapping region. It is also observed in both ABCD and EFGH regions that even the number of such subregions vary between the horizontal and vertical profile generation. These profiles help in determining the pattern in which the input elevation values are transformed. The weights of both vertical and horizontal blend methods ensure a seamless elevation transition between the rows of the path and across the paths, respectively. From the above analysis over ABCD and EFGH regions, without loss of generality, we hypothesize that the analysis holds valid to the remaining overlapping regions of the ROI A'B'C'D'.

4.3.3. Elevation consistency

This section presents the relative consistency in the elevation values of the Cartosat-1 DEM mosaic outputs with SRTM DEM. The outputs from three methods are resampled from 10 m to 30 m using bilinear interpolation, to compare with SRTM DEM (30 m). Table 1 provides the mean absolute error (MAE) and root mean square error (RMSE) of three resampled DEMs with SRTM DEM over ABCD, EFGH, and A'B'C'D' regions. The MAE and RMSE of the elevation values from average and proposed methods are very close over ABCD, EFGH, and A'B'C'D' regions. These metrics also determine the closeness of the transformed elevation values to SRTM DEM.

4.3.4. Terrain ruggedness index

This section presents a quantitative analysis on the DEM mosaic outputs by determining their smoothness using terrain ruggedness index (TRI), a measurement described in Riley et al. (1999). The process of obtaining TRI starts by computing the elevation differences between the center cell (u, v) and its eight adjacent cells. Then by calculating the average of the squares of each of the eight elevation difference values. Finally, the square root of this average represents TRI value of the center cell (u, v). The TRI of a DEM mosaic output is obtained by iterating the same process over each cell. Eq. (26) represents TRI calculation over a center cell (u, v).

$$I'(u, v) = \sqrt{\left(\frac{1}{8} \sum_{i=-1}^1 \sum_{j=-1}^1 [I(u+i, v+j) - I(u, v)]^2\right)} \tag{26}$$

where I(u, v) and I'(u, v) represent the DEM mosaic output and its TRI, respectively.

We consider mean TRI as an indicator to measure the smoothness of the mosaic output. The mosaic outputs obtained from three mosaic methods over A'B'C'D' region are cropped to the extents of individual DEM scenes. Now, mean TRI is calculated over each of these cropped mosaic outputs. Each individual scene has its own elevation range, which helps to evaluate the performance of mosaic methods over different terrains quantitatively. Fig. 16 shows the performance of mosaic methods over 40 differ terrains in terms of mean TRI. The elevation range of each original input DEM scene is indicated by a numerical value on top of each bar. The proposed method outperforms other two

Table 1
Comparison of elevation statistics of Cartosat-1 DEM mosaic outputs with SRTM DEM over three regions.

Region	$MAE^a(m)$			$RMSE^b(m)$		
	Average	Feathering-based	Proposed	Average	Feathering-based	Proposed
ABCD	2.4889	3.0536	2.5316	3.2486	3.7861	3.2997
EFGH	2.5562	3.7962	2.5824	3.3615	4.7929	3.3251
A'B'C'D'	2.5833	2.8038	2.5613	3.4676	3.8167	3.3978

$$^a MAE = \frac{1}{n} \sum_{i=1}^n |s_i - m_i|;$$

$$^b RMSE = \sqrt{\frac{1}{n} \sum_{i=1}^n (s_i - m_i)^2}; \text{ where } s_i \text{ and } m_i \text{ represent elevation values of SRTM and mosaic output, respectively.}$$

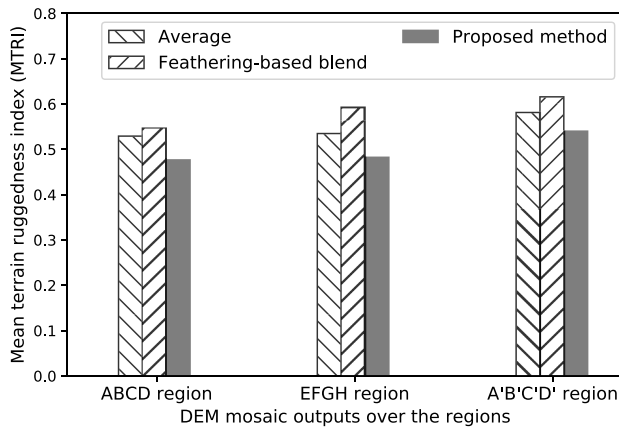


Fig. 17. Comparison of mean terrain ruggedness index of DEM mosaic outputs from three methods over *ABCD*, *EFGH*, and *A'B'C'D'* regions.

mosaic methods based on their mean TRI values. Also, demonstrates its consistency over different terrain regions whose elevation ranges vary from 31 m to 520 m.

Fig. 17 provides a quantitative analysis over the three methods in terms of mean TRI, which determines the smoothness of their DEM mosaic outputs. From **Fig. 17**, it is evident that the mosaic output from the proposed method exhibits smoothness compared to average method and feathering-based blend method.

5. Conclusion and future work

In this paper, we proposed a novel framework to create a seamless DEM mosaic from the Cartosat-1 input DEM scenes. We employed the metadata of the input scenes to determine their sequence during the mosaic process. A suitable weights derivation mechanism is formulated to handle all possible cases of DEM overlaps. The proposed framework exhibits a smooth transition of the elevation values in the overlapping regions in comparison with the average and conventional feathering-based blend methods. Also, the proposed method demonstrates its efficacy on all kinds of terrains. Though the region of interest considered for our experiment is of $1^\circ \times 1^\circ$, the proposed framework is applicable to any extent of the study area. This framework produces a high-quality seamless Cartosat-1 DEM mosaic, which is suitable for a wide range of hydro-logical and geomorphological applications. In future, we make use of these DEM mosaic outputs as the contextual information for the objects to describe their attributes.

CRedit authorship contribution statement

Rajeshreddy Datla: Problem identification, Conceptualization, Data curation, Methodology, Implementation, Original draft preparation, Software. **C. Krishna Mohan:** Supervision, Critically revisiting the manuscript.

Declaration of competing interest

The authors declare that they have no known competing financial interests or personal relationships that could have appeared to influence the work reported in this paper.

Acknowledgments

The authors would like to thank Raghu Venkataraman, Director, ADRIN, and Dr.P.V.Radha devi, Deputy Director (GPAA), ADRIN, Secunderabad, for their encouragement. Team bundle block adjustment project, ADRIN, Secunderabad, is also thanked for their support for this work. This research did not receive any specific grant from funding agencies in the public, commercial, or not-for-profit sectors.

Computer code availability

Name of code: DEMOverlap_mosaic

Name of the Developer: Rajeshreddy Datla

Contact address: Signal processing division, Advanced Data Processing Research Institute (ADRIN), Dept of Space, Government of India, Akbar Road, Tarbund, Manovikas Nagar, Secunderabad 500009, India
Telephone number: +919704143731

E-mail: rajesh@adrin.res.in

Year first available: 2019

Hardware required:

Processor: Intel Xeon Processor and above

RAM: 8 GB minimum. Hard disk: 60 GB minimum.

Software required:

C++ IDE for 64-bit Windows 10 OS

(E.g., Microsoft Visual Studio 2010); Programming language: C++;

Program size = 30 MB;

Source code is available at <https://github.com/RAJESH DATLA/Cartosat-1-DEM-Mosaic>

References

- Aher, S., Kantamaneni, K., Deshmukh, P., 2017. Detection and delineation of water bodies in hilly region using CartoDEM, SRTM and ASTER GDEM data. *Remote Sens. Land 1* (1), 41–52. <http://dx.doi.org/10.21523/gcjl.17010103>.
- Akilan, A., Nagasubramanian, V., AnkitChaudhry, RajeshReddy, D., SudheerReddy, D., UshaDevi, R., Tirupati, T., Radhadevi, P.V., GeetaVaradan, 2014. Effective system for automatic bundle block adjustment and ortho image generation from multi sensor satellite imagery. In: *International Archives of the Photogrammetry, Remote Sensing and Spatial Information Sciences, ISPRS Technical Commission VIII Symposium*, Vol. XL-8. pp. 1091–1094. <http://dx.doi.org/10.5194/isprsarchives-XL-8-1091-2014>.
- Amitabh, S., Gopala Krishna, B., Srinivasan, T.P., Srivastava, P.K., 2011. A comparative study between forward and reverse stereos of Cartosat-1. In: *National Conference on Impact of Climate Change with Special Emphasis on Desertification and Special Session on Technological Trends in Geomatics, Ajmer*.
- Amitabh, Gopala Krishna, B., Srivastava, P.K., 2009. Extraction of 3D geo-information from Cartosat images and its visualisation. In: *Joint International Workshop of ISPRS WG IV/1, WG IV/3 and WG VIII/1 on Geospatial Data Cyber Infrastructure and Real-time Services with Special Emphasis on Disaster Management*. INCOIS, Hyderabad.
- Amitabh, Krishna, B.G., Srinivasan, T., Srivastava, P., 2008. An integrated approach for topographical mapping from space using Cartosat-1 and Cartosat-2 imagery. *Int. Arch. Photogramm. Remote Sens. Spat. Inf. Sci. XXXVIII (B4)*, 1354–1358.

- Astrid, G., Birgit, W., Michele, M., Achim, R., 2016. The TanDEM-x DEM mosaicking: Fusion of multiple acquisitions using inSAR quality parameters. *IEEE J. Sel. Top. Appl. Earth Obs. Remote Sens.* 9 (3), 1047–1057. <http://dx.doi.org/10.1109/JSTARS.2015.2421879>.
- Bhandari, R., Shweta, S., Pathan, S., 2006. Derivation of building footprints and 3D city modeling using Cartosat-1 stereo data. *NNRMS Bull.* 31, 41–46.
- Bhardwaj, A., Snehmami, Pandit, A., Ganju, A., 2014. Demarcation of potential avalanche sites using remote sensing and ground observations: a case study of gangotri glacier. *Geocarto Int.* 29 (5), 520–535. <http://dx.doi.org/10.1080/10106049.2013.807304>.
- Bhatt, C., Rao, G., 2016. Ganga floods of 2010 in uttar pradesh, north India: a perspective analysis using satellite remote sensing data. *Geomatics, Natural Hazards and Risk* 7 (2), 747–763. <http://dx.doi.org/10.1080/19475705.2014.949877>.
- Binoy, B.V., Shashank, B., Hebbar, R., Raj, U., Karuppasamy, S., 2014. Virtual 3D mapping and analysis using remote sensing data and photographs. *International Journal of Remote Sensing and Geoscience (IJRSG)* (ISSN: 2319-3484) 3 (5), 42–46.
- Boyko, B.B., 2007. Representing trees. In: *Mathematics and Education in Mathematics, Proc. 36th Spring Conf. of the Union of Bulgarian Mathematicians*. pp. 193–196.
- Buhler, Y., Kumar, S., Veitinger, J., Christen, M., Stoffel, A., Snehmami, 2013. Automated identification of potential snow avalanche release areas atmospheric measurement based on digital elevation models. *Nat. Hazards Earth Syst. Sci.* 13, 1321–1335. <http://dx.doi.org/10.5194/nhess-13-1321-2013>.
- Dahatonde, A., Khatik, A., Patil, A., Zodape, P., 2016. Building detection in urban area from Cartosat-1. *Int. J. Adv. Res. Comput. Eng. Technol. (IJARCET)* 5 (4), 988–993.
- Dong, L., Shan, J., 2013. A comprehensive review of earthquake-induced building damage detection with remote sensing techniques. *ISPRS J. Photogramm. Remote Sens.* 84, 85–99. <http://dx.doi.org/10.1016/j.isprsjprs.2013.06.011>.
- ESRI, 2011. *ArcGIS Desktop: Release*. ESRI, Redlands, CA, p. 10.
- Geiss, C., Aravena Pelizari, P., Marconcini, M., W., S., Edwards, M., Lakes, T., Taubenböck, H., 2015. Estimation of seismic building structural types using multi-sensor remote sensing and machine learning techniques. *ISPRS J. Photogramm. Remote Sens.* 104, 175–188. <http://dx.doi.org/10.1016/j.isprsjprs.2014.07.016>.
- Ghosh, D., Kaabouch, N., 2016. A survey on image mosaicing techniques. *J. Visula Commun. Image Represent.* 34, 1–11. <http://dx.doi.org/10.1016/j.jvcir.2015.10.014>.
- Giribabu, D., 2014. Generation of statewide DEMs and orthoimages guidelines and methodology. *Kartogr. geoinf. (Cartogr. Geoinf.)* 13 (22), 4–19.
- Giribabu, D., Srinivasa Rao, S., Murthy, Y.K., 2013. Improving Cartosat-1 DEM accuracy using synthetic stereo pair and triplet. *ISPRS J. Photogramm. Remote Sens.* 77, 31–43. <http://dx.doi.org/10.1016/j.isprsjprs.2012.12.005>.
- Harrington, S., 1983. *Computer Graphics: A Programming Approach*. Mc Graw Hill.
- Hsu, C., Wu, J., 1996. Multiresolution mosaic. *IEEE Trans. Consum. Electron.* 42 (4), 981–990. <http://dx.doi.org/10.1109/30.555800>.
- Jacobsen, K., Crespi, M., Fratarcangeli, F., Giannone, F., 2008. DEM generation with Cartosat-1 stereo imagery. In: *Proceedings of EARSeL Joint Workshop on Remote Sensing - New Challenges of High Resolution*, Bochum., pp. 40–47.
- Jain, D., Rao, C., Kumar, S., Suresh, S., 2008. Assessment of DEM mosaic accuracy. *Int. Arch. Photogramm. Remote Sens. Spat. Inf. Sci.* XXXVII, 1137–1141.
- Knöpfle, Strunz, W., A., G.R., 1998. Mosaicking of digitalelevation models derived by SAR interferometry. *Int. Arch. Photogramm. Remote Sens.* 32 (Part 4), 306–313.
- Krieger, G., Moreira, A., Fiedler, H., Hajnsek, I., Werner, M., Younis, M., Zink, M., 2007. TanDEM-X: a satellite formation for high-resolution SAR interferometry. *IEEE Trans. Geosci. Remote Sens.* 45, 3317–3341.
- Leitão, J., Prodanović, D., Maksimović, C., 2016. Improving merge methods for grid-based digital elevation models. *Comput. Geosci.* 88, 115–131. <http://dx.doi.org/10.1016/j.cageo.2016.01.001>.
- Martha, T.R., Kerle, N., Jetten, V., van Westen, C.J., Vinod, K., 2010. Landslide volumetric analysis using Cartosat-1-derived DEMs. *IEEE Geosci. Remote Sens. Lett.* <http://dx.doi.org/10.1109/LGRS.2010.2041895>.
- Milgram, D., 1975. Computer methods for creating photomosaics. *IEEE Trans. Comput.* 24 (11), 1113–1119. <http://dx.doi.org/10.1109/T-C.1975.224142>.
- Milgram, D., 1977. Adaptive techniques for photomosaicking. *IEEE Trans. Comput.* 26 (11), 1175–1180. <http://dx.doi.org/10.1109/TC.1977.1674772>.
- NRSA, 2006. *CARTOSAT-1 data user's handbook*. URL: www.euromap.de/download/p5_data_user_handbook.pdf.
- NRSC, I., 2013. *Technical Methodology for Countrywide DEM and Ortho Product Generation for India using Cartosat-1 stereo data*. Technical Report, NRSC, ISRO.
- NRSC, I., 2015. *Cartosat-1 10 Years and Beyond*. Technical Report, NRSC, ISRO.
- Pal, S., Saha, T.K., 2017. Exploring drainage/relief-scape sub-units in atreyee river basin of India and Bangladesh. *Spat. Inf. Res.* <http://dx.doi.org/10.1007/s41324-017-0133-3>.
- Prashantha, K., 2017. Capability of Cartosat-1 stereo image data for integrated watershed management. *International Journal of Current Engineering and Scientific Research (IJCESR)* (ISSN: 2393-8374) 4 (11), 12–20.
- Radhadevi, P.V., Nagasubramanian, V., Mahapatra, A., Solanki, S.S., Sumanth, K., Varadan, G., 2009. Potential of high-resolution Indian remote sensing satellite imagery for large scale mapping. In: *ISPRS HannoverWorkshop, High Resolution Earth Imaging for Geospatial Information*, Vol. XXXVIII-1-4-7/W5. pp. 2–5.
- Rajpriya, N.R., Anjana, V., Sharma, S.A., 2014. Generation of 3D model for urban area using IKONOS and Cartosat-1 satellite imageries with RS and GIS techniques. In: *ISPRS - International Archives of the Photogrammetry, Remote Sensing and Spatial Information Sciences*, Vol. XL. ISPRS, Hyderabad, India, pp. 899–906. <http://dx.doi.org/10.5194/isprarchives-XL-8-899-2014>.
- Ramesh, L., Dikpal, T.J., Renuka Prasad, K.S., 2017. Evaluation of morphometric parameters derived from Cartosat-1 DEM using remote sensing and GIS techniques for budigere amaniere watershed, dakshina pinakini basin, karnataka, India. *Appl. Water Sci.* 7, 4399–4414. <http://dx.doi.org/10.1007/s13201-017-0585-6>.
- Rao, C.V., Sathyanarayana, P., Jain, D.S., Manjunath, A.S., 2007. *Topographic map updation using Cartosat-1 data*. In: 2007 Annual Conference of the Remote Sensing & Photogrammetry Society, RSPSoc2007. on CDROM, Newcastle upon Tyne, UK.
- Reuter, H., Hengl, T., Gessler, P., Soille, P., 2009. Preparation of DEMs for geomorphometric analysis. *Geomorphometry: Concepts, Software, Applications. Developments in Soil Science* 33, 87–120. [http://dx.doi.org/10.1016/S0166-2481\(08\)00004-4](http://dx.doi.org/10.1016/S0166-2481(08)00004-4).
- Riley, S.J., DeGloria, S., Elliot, R., 1999. A terrain ruggedness index that quantifies topographic heterogeneity. *Interm. J. Sci.* 5 (1–4), 23–27.
- Robinson, N., Regetz, J., Guralnick, R., 2014. Earthen-DEM90: A nearly-global, void-free, multi-scale smoothed, 90m digital elevation model from fused ASTER and SRTM data. *ISPRS J. Photogramm. Remote Sens.* 87, 57–67. <http://dx.doi.org/10.1016/j.isprsjprs.2013.11.002>.
- Roth, W.K., Rabus, B., Gebhardt, S., Scales, D., 1999. Gemos a system for the geocoding and mosaicking of interferometric digital elevation models. In: *IEEE 1999 International Geoscience and Remote Sensing Symposium. IGARSS'99*. IEEE, Hamburg, Germany, <http://dx.doi.org/10.1109/IGARSS.1999.774553>.
- Sharma, A., Kartikeyan, B., 2014. Potential of CartoDEM in disaster management. *J. Geomat.* 8 (1), 96–100, URL: <https://www.isgindia.org/JOG/abstracts/april-2014/16.pdf>.
- Simhadri, R.B., Suresh Babu, A.V., Shanker, M., Venkateswar, R.V., 2013. Remote sensing inputs for feasibility assessment studies of proposed water resources projects. *NNRMS Bulletin* 38, 117–123.
- Steve, D., Heidrun, S., 2017. Visualization of features in 3D terrain. *ISPRS Int. J. Geo-Inf.* 6, 1–20. <http://dx.doi.org/10.3390/ijgi6110357>.
- Tack, F., Buyuksalih, G., Goossens, R., 2012. 3D Building reconstruction based on given ground plan information and surface models extracted from spaceborne imagery. *ISPRS J. Photogramm. Remote Sens.* 67, 52–64. <http://dx.doi.org/10.1016/j.isprsjprs.2011.10.003>.
- Tian, J., Reinartz, P., d'Angelo, P., Ehlers, M., 2013. Region-based automatic building and forest change detection on Cartosat-1 stereo imagery. *ISPRS J. Photogramm. Remote Sens.* 79, 226–239. <http://dx.doi.org/10.1016/j.isprsjprs.2013.02.017>.
- Warriner, T., Mandlbürger, G., 2005. Generating a new high resolution DTM product from various data sources. In: *Fritsch, D. (Ed.), 50th Photogrammetric Week. Wichmann Verlag, Heidelberg*, pp. 197–206.
- Wilkinson, B., DeWitt, B., Wolf, P., 2014. *Elements of Photogrammetry with Application in GIS*, fourth ed. McGraw-Hill Education, URL: <https://books.google.co.in/books?id=741SXwAACAAJ>.
- Zink, M., Bachmann, M., Brautigam, B., Fritz, T., Hajnsek, I., Moreira, A., Wessel, B., Krieger, G., June 2014. TanDEM-X: the new global DEM takes shape. *IEEE Trans. Geosci. Remote Sens. Mag.* 2 (2), 8–23. <http://dx.doi.org/10.1109/MGRS.2014.2318895>.